ADVANCING EARTH AND SPACE SCIENCE

Earth and Space Science

RESEARCH ARTICLE
10.1029/2022EA002253

**Key Points:**

- This study integrates recent advances in fault-based seismic hazard assessment with the Epidemic-Type Aftershock Sequence model
- Fault-based seismic hazard assessment produces different ground-motion estimates compared to conventional hazard assessment approaches
- Close to modeled faults, the influence of aftershock inclusion on seismic hazard estimates is generally highest for low return periods

**Supporting Information:**

Supporting Information may be found in the online version of this article.

**Correspondence to:**

S. Iacoletti,
salvatore.iacoletti.19@ucl.ac.uk

**Citation:**

Iacoletti, S., Cremen, G., & Galasso, C. (2022). Integrating long and short-term time dependencies in simulation-based seismic hazard assessments. *Earth and Space Science*, *9*, e2022EA002253. https://doi.org/10.1029/2022EA002253

Received 20 JAN 2022
Accepted 11 AUG 2022

**Author Contributions:**

**Conceptualization:** Salvatore Iacoletti, Gemma Cremen, Carmine Galasso
**Data curation:** Salvatore Iacoletti
**Formal analysis:** Salvatore Iacoletti, Gemma Cremen
**Funding acquisition:** Carmine Galasso
**Investigation:** Salvatore Iacoletti, Gemma Cremen
**Methodology:** Salvatore Iacoletti, Gemma Cremen, Carmine Galasso
**Project Administration:** Carmine Galasso



# Integrating Long and Short-Term Time Dependencies in Simulation-Based Seismic Hazard Assessments

**Salvatore Iacoletti[1], Gemma Cremen[1], and Carmine Galasso[1,2]**

[1]Department of Civil, Environmental and Geomatic Engineering, University College London, London, UK, [2]Scuola Universitaria Superiore (IUSS) Pavia, Pavia, Italy

**Abstract** Conventional probabilistic seismic hazard analysis (PSHA) only considers mainshock events and uses a time-independent earthquake rupture forecast to describe the occurrence of mainshocks. This approach neglects the long-term time-dependency of mainshocks on specific fault segments, the interaction of adjacent faults, and the spatial and temporal clustering of aftershocks. This study integrates a recently proposed advanced fault-based PSHA framework with an aftershock simulator based on the Epidemic-Type Aftershock Sequence (ETAS) model, to overcome the aforementioned limitations. Central Italy is used as a case study to illustrate the proposed framework. The case-study hazard curves show that including state-of-the-art advances in fault-based PSHA may increase the ground-motion amplitudes for low return periods, and decrease the ground-motion amplitudes for high return periods, relative to a conventional PSHA approach. The magnitude of ground-motion estimate increases due to aftershock inclusion is dependent on the selected site and return period. Sensitivity analyses of the results demonstrate that: (a) close to modeled faults, high-return-period hazard estimates are more affected by fault-related inputs than the aftershock inclusion; (b) close to modeled faults, the influence of aftershock inclusion is higher for low return periods than high ones; (c) away from modeled faults, aftershocks inclusion greatly affects the variance of the hazard results; and (d) fault interaction has a limited effect on the variance of the hazard estimates compared to other analysis inputs. This study could help with the future implementation of complex fault modeling approaches and aftershock hazard in seismic risk models.

**Plain Language Summary** State-of-practice seismic hazard assessments do not usually consider the actual geometry of the faults, the time at which earthquakes occurred in the past, and the elevated hazard due to aftershocks. This study proposes a framework to address these shortcomings, which is demonstrated through a case study involving several sites in Central Italy. The case-study results demonstrate how conventional estimates of earthquake hazard can be affected by using state-of-the-art methodologies to model faults and aftershocks. In particular, complex fault modeling can increase the seismic hazard for low return periods, and decrease the seismic hazard for high return periods, relative to a conventional hazard estimation approach. The inclusion of aftershocks increases seismic hazard as expected, but the size of the increase is highly dependent on the selected site and the return period of ground shaking. This study could help the future implementation of more complex hazard modeling approaches in earthquake risk assessments.

## 1. Introduction

Probabilistic seismic hazard analysis (PSHA) at a site estimates the probability that an earthquake-induced ground-motion intensity measure (IM) (e.g., peak ground acceleration) exceeds a given value during a specified time window (McGuire, 2004). Traditionally, PSHA applications have considered a time-independent (i.e., Poissonian) earthquake rupture forecast (ERF) with simplified area sources to describe the effects of ground shaking from declustered (i.e., mainshock) seismicity (e.g., SSHAC, 1997). This approach: (a) ignores pertinent fault features (e.g., geometries); and (b) neglects seismicity due to aftershocks.

Several recent earthquake events (e.g., the 2016 moment magnitude—$M_W$—7.8 Kaikōura earthquake, New Zealand and the 2019 $M_W$ 6.4–7.1 Ridgecrest sequence, USA) highlighted the need to explicitly account for fault sources in PSHA. As pointed out by several authors, fault-based ERF models enable more detailed descriptions of the hazard due to known fault segments (e.g., Field et al., 2014; Stirling et al., 2012), taking full advantage of active fault databases and seismological data. Iacoletti et al. (2021) recently unified state-of-the-art advances in fault-based PSHA within a single harmonized framework. The framework incorporates some underlying

**Resources:** Salvatore Iacoletti, Gemma Cremen
**Software:** Salvatore Iacoletti
**Supervision:** Gemma Cremen, Carmine Galasso
**Validation:** Salvatore Iacoletti, Gemma Cremen
**Visualization:** Salvatore Iacoletti, Gemma Cremen, Carmine Galasso
**Writing – original draft:** Salvatore Iacoletti, Gemma Cremen, Carmine Galasso
**Writing – review & editing:** Salvatore Iacoletti, Gemma Cremen, Carmine Galasso

methodologies of the latest Uniform California Earthquake Rupture Forecast (UCERF3; Field et al., 2014), providing a comprehensive means of relaxing fault segmentation (i.e., how faults are translated into seismogenic sources), accounting for multi-segment ruptures in a standardized way, interpreting available fault data in a consistent manner, and inferring time-dependent probabilities of mainshock occurrence (Field et al., 2015). It also explicitly incorporates fault-interaction triggering between major known faults, using the approach outlined by Mignan et al. (2016) and Toda et al. (1998). The framework by Iacoletti et al. (2021) exclusively focuses on fault-based mainshock hazard, neglecting lower-magnitude seismicity and earthquakes caused by blind or unknown faults that are crucial for a complete assessment of the hazard (e.g., Stirling et al., 2012). These types of earthquakes can be captured using a time-independent distributed seismicity model (e.g., Field et al., 2014; Stirling et al., 2012).

Most PSHA approaches, including that of Iacoletti et al. (2021), do not account for aftershock events. Several authors pointed out that these events are also important to consider because: (a) they can produce similar or larger ground-motion intensities compared to their corresponding mainshocks (e.g., Boyd, 2012; Marzocchi & Taroni, 2014); and (b) even aftershock ground-motion intensities smaller than those of the mainshock can be damaging due to the increased vulnerability of a building stock/infrastructure system after the main event (e.g., Gentile & Galasso, 2021; Hatzigeorgiou & Beskos, 2009). For example, the $M_W$ 6.2 Christchurch earthquake in 2011 was an aftershock that caused higher ground-motion intensities and higher economic losses than the corresponding $M_W$ 7.1 mainshock (Kam et al., 2011; Potter et al., 2015). Many analytical frameworks for incorporating aftershocks in seismic hazard assessments have already been proposed in the literature. Yeo and Cornell (2009), for instance, developed aftershock probabilistic seismic analysis (APSHA) that uses a nonhomogeneous Poisson model to estimate aftershock occurrence and the modified Omori's law (Utsu et al., 1995) to calculate the occurrence rate. Boyd (2012) proposed a methodology that considers the mainshock and associated aftershocks as time-independent clusters. Each cluster has the recurrence time of the mainshock, and aftershock events can contribute to ground-motion intensity at a given site. Iervolino et al. (2014) proposed an analytical method that uses the modified Omori's law to incorporate aftershocks in hazard calculations. Yaghmaei-Sabegh et al. (2017) proposed a methodology similar to that of Iervolino et al. (2014), based instead on the Epidemic-Type Aftershock Sequence (ETAS) model (Ogata, 1998; Zhuang et al., 2011). However, all of these methodologies assume a simplistic time-independent rupture occurrence model for the mainshocks.

This study aims to develop a comprehensive approach to PSHA that addresses the aforementioned limitations associated with state-of-the-art seismic hazard assessments. The fault-based PSHA framework in Iacoletti et al. (2021) is extended by adding: (a) a distributed seismicity occurrence model; and (b) an ETAS-based aftershock simulator (based on the findings of Iacoletti et al., 2022) for incorporating aftershocks in the stochastic event sets. The proposed approach is simulation-based, which involves stochastically generating event sets for a given time span (e.g., Pagani et al., 2014). This type of analysis is generally more flexible than analytical approaches and can easily integrate aftershock modeling with long-term (i.e., time window of decades) time-dependent hazard estimates. A simple case study based on 43 fault segments located in Central Italy is established to explore the effect of increasing modeling complexity and aftershock inclusion. The sensitivity of the hazard estimates (i.e., ground-motion intensity for specific return periods) to the segmentation assumptions, long-term rupture occurrence model, interaction amongst faults, and aftershock inclusion are also investigated.

This study is organized as follows. Section 2 develops and discusses the proposed simulation-based framework for comprehensive seismic hazard assessment. Section 3 demonstrates a case-study application of the framework to the Central Italy area. Sections 4 and 5 provide discussion and conclusions, respectively.

## 2. Methodology

Figure 1 provides a flowchart of the proposed simulation-based PSHA approach. Mainshocks are generated through the fault-based and distributed seismicity modules (i.e., the mainshock stochastic event set generator). Aftershocks are then simulated for each mainshock with an ETAS-based short-term aftershock simulator, to complete the stochastic event set. Finally, the parameters of each event and location of interest are input to a set of ground-motion and correlation (both spatial and cross-intensity measure) models, which are used to produce the hazard curves.

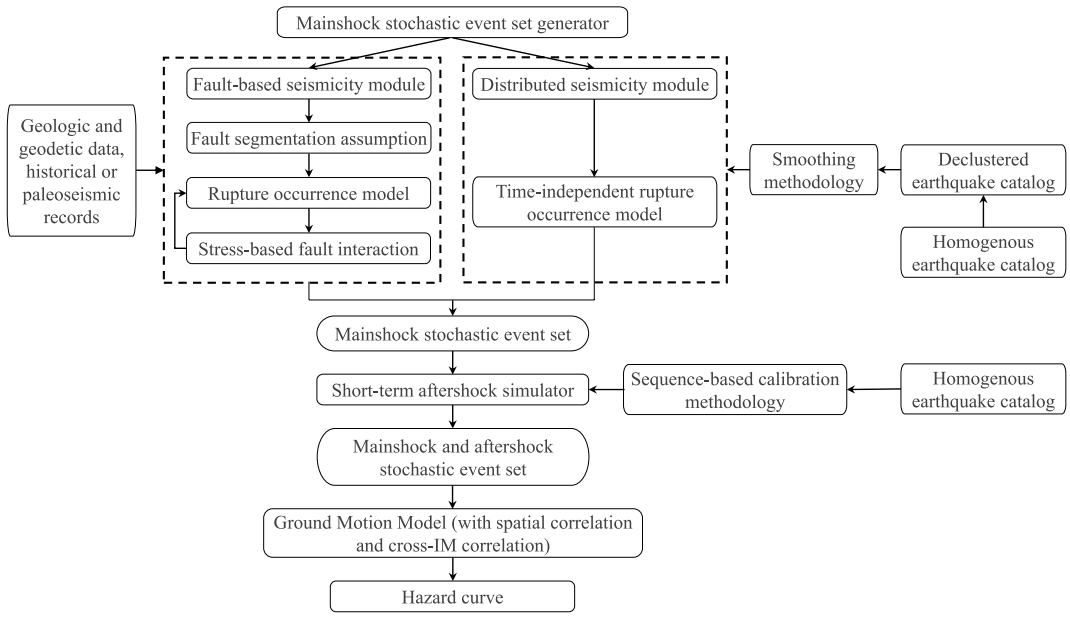


**Figure 1.** Flowchart of the proposed framework for comprehensive simulation-based probabilistic seismic hazard analysis (PSHA).

### 2.1. Mainshock Stochastic Event Set Generator

#### 2.1.1. Fault-Based Seismicity Module

The fault-based seismicity module uses geologic and geodetic data with any available information on historical and paleoseismic records to model large magnitude ruptures that the considered fault system can generate. The fault-based seismicity module is derived from the framework proposed by Iacoletti et al. (2021), which is based upon previous work by Field et al. (2014), Field et al. (2015), Mignan et al. (2016), and Toda et al. (1998). The framework can incorporate different modeling assumptions regarding: (a) the segmentation of fault segments; (b) the rupture occurrence probability model; and (c) fault interaction, all of which are investigated as part of the sensitivity analyses in Section 2.4. Interested readers are referred to Iacoletti et al. (2021) for details of the framework implementation, which consists of the following steps (described here in brief):

1. Rupture generation: based upon the characteristics of the considered fault system, this step produces a set of physically possible ruptures following the unsegmented approach proposed for UCERF3 (Field et al., 2014). This means that the ruptures include floating (i.e., the rupture area is smaller than the whole fault segment surface) and multi-segment rupture earthquakes (i.e., involving more than one fault segment);
2. Inversion: this step calibrates the long term time-independent rates, $\lambda_r$, of all the ruptures from the previous step. This is achieved by synthesizing all the available information for the considered fault segments (slip rates, paleoseismic/historical records, slip models, magnitude-frequency distribution shape, rate smoothing along a fault segment) as constraints of an optimization problem. Paleoseismic data are interpreted for each available investigation site (or aggregated across only nearby sites) and are associated with the closest point of the considered fault (Field et al., 2015). The inversion methodology in Iacoletti et al. (2021) incorporates the following types of segmentation model: (a) a fully segmented rupture model (*SRM*), which uses the characteristic earthquake magnitude assumption (Schwartz & Coppersmith, 1984); (b) a no multi-segment model (*NMM*), which limits ruptures within geological boundaries and prevents them from "jumping" from one fault segment to another (but floating ruptures are still allowed to occur); and (c) an unsegmented rupture model (*URM*), where both multi-segment ruptures and floating ruptures can occur;
3. Occurrence probability calculation: two different rupture occurrence models can be considered as part of this step: (a) time-independent (Poissonian) model, characterized by one parameter (the long-term mean recurrence time); and (b) time-dependent Brownian Passage Time (BPT, Matthews et al., 2002) model, characterized by two parameters (the mean recurrence time, $\mu$, and the aperiodicity $\alpha$). Three sets of magnitude-dependent aperiodicities (proposed by Field et al., 2015) with increasing level of recurrence uncertainty (i.e., low, mid,

and high uncertainty) are used in this study, but any other set could theoretically be incorporated. Traditionally, occurrence models are applied to segmented faults under the hypothesis that the same earthquake occurrence model is valid for each point of a fault segment (e.g., Akinci et al., 2009). However, Field (2015) shows that commonly adopted occurrence models (e.g., Poissonian and BPT, amongst others) cannot be applied to specific fault points. Therefore, this study follows the unsegmented approach of UCERF3 and applies occurrence models to ruptures instead of points on faults (details in Iacoletti et al., 2021). In this context, the parameters of the occurrence models are not directly comparable to segmented cases (Field et al., 2015);

4. Fault interaction: this step incorporates a fault interaction proxy (i.e., Coulomb stress changes, King et al., 1994) that updates the occurrence probabilities computed in the previous step. Fault interaction can be applied with both time-dependent and time-independent rupture occurrence models.

#### 2.1.2. Distributed Seismicity Module

The distributed seismicity module models the occurrence of moderate-to-large earthquakes (i.e., $M_W \geq 5$ in this study), as well as earthquakes from blind or unknown fault segments. It consists of gridded point sources with individual Gutenberg-Richter (GR, Gutenberg & Richter, 1944), magnitude-frequency distributions (MFDs).

The time-independent rate, $\lambda_{c,r}$, of all point ruptures (i.e., with no surface geometry) for each cell of the grid is computed with the procedure detailed in Supporting Information S1. This procedure applies Frankel (1995)'s smoothing technique on the declustered catalog (the declustering algorithm by Gardner & Knopoff, 1974, is used in this study) over a given grid of points. The MFD for each cell is built by computing the *b*-value and the maximum magnitude.

To avoid double-counting events where point sources and fault ruptures overlap, the implemented procedure (see Supporting Information S1 for full details): (a) removes events in the catalog associated with known faults if their $M_W$ is higher than the minimum magnitude considered in the fault-based seismicity module (e.g., Valentini et al., 2019); and (b) applies the methodology described by Powers and Field (2013) for cells that spatially overlap with the fault geometries in the fault-based seismicity module. This involves defining additional MFDs with a maximum magnitude equal to the minimum magnitudes of the possible ruptures generated by the fault segments. The final MFD for each overlapping cell is then computed through a weighted average of the associated MFDs, based on the extent of the overlapping areas. In this study, the empirical depth distribution is derived from the earthquake catalog and the empirical focal mechanism distribution is taken from previously published sources. The $\lambda_{c,r}$ values of all point ruptures are generated from the GR MFD, the depth empirical distribution and the focal mechanism empirical distribution, respectively. Further details are provided in Supporting Information S1.

#### 2.1.3. Combined Mainshock Event Set Generation

The event simulation methodology of Iacoletti et al. (2021) is used in this study. This methodology generates the time of the events $t_i$ on a yearly basis (in decimal years). 100,000 one-year long mainshock stochastic event sets are simulated separately from the fault-based seismicity module and the distributed seismicity module (i.e., the two modules are considered independent during the simulation phase, see Figure 2). The two stochastic event sets are then unified and simulated events are sorted in chronological order.

Figure 2 shows how the rate of each rupture is calculated at every step of the simulation (i.e., when an event is generated in the stochastic event set). For the fault-based seismicity module and a time-independent rupture occurrence assumption, each rupture's rate is equal to $\lambda_r$ of Section 2.1.1. If the time-dependent rupture occurrence model is assumed instead, the time elapsed since the last event is updated according to the procedure in Iacoletti et al. (2021) and the equivalent time-dependent rate $\lambda_{eq,r}$ is calculated through a non-homogeneous Poisson process (Convertito & Faenza, 2014):

$$\lambda_{eq,r} = -\log(1 - P_r)/w \tag{1}$$

where $P_r$ is the conditional probability of occurrence of the *r*th rupture, $w$ is the observation window, which is either one year (if no event is simulated within the considered year) or $1-\sum t_i$ (otherwise). If fault interaction is considered, the rates $\lambda_r$ or $\lambda_{eq,r}$ are modified according to the formulations in Appendix D of Iacoletti et al. (2021) to compute $\lambda_{r,fi}$. The time-independent rupture occurrence model (with no fault interaction) is always used for the distributed seismicity module, and each rupture's rate is equal to $\lambda_{c,r}$ of Section 2.1.2.

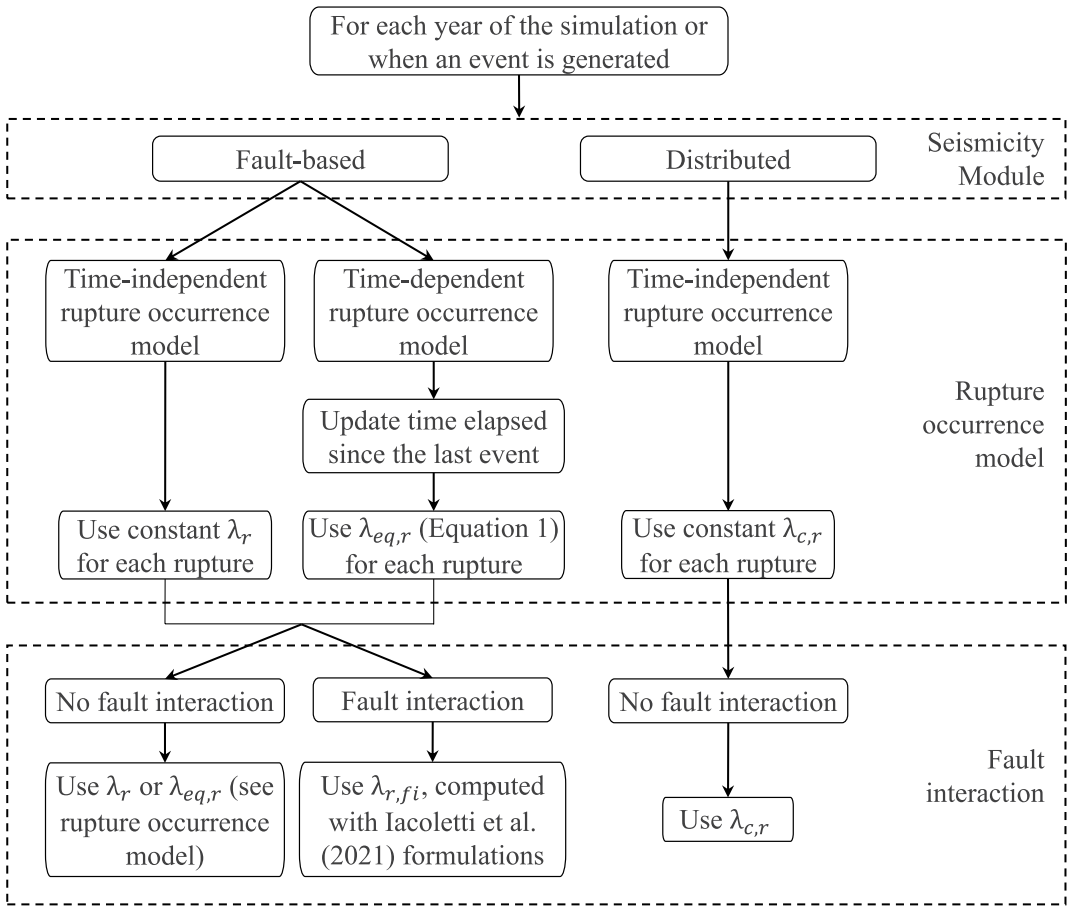


**Figure 2.** Flowchart of long-term (mainshock) rate calculation for each step of the simulation (i.e., when an event is generated in the stochastic event set).

### 2.2. Aftershock Simulation Methodology

The aftershock simulator produces aftershocks conditional on the generated mainshocks (Section 2.1). The ETAS-based formulation in Iacoletti et al. (2022) is used as the aftershock simulator for the proposed framework. It is similar to the original ETAS formulations by Ogata (1998) and Zhuang et al. (2011), but also includes the aftershock temporal probability density function (PDF; details to follow), the truncated GR distribution, finite fault model geometries (where available), and the short-term variation of the completeness magnitude after large $M_W \geq 6$ mainshocks. The required input parameters of the model are: $A$ and $\alpha$, which control the average number of aftershocks associated with the $i$th parent mainshock of magnitude $m_i$; $c$ and $p$, which define the PDF of the occurrence time of an aftershock event relative to the time $t_i$ of the parent mainshock (this PDF is referred to as the aftershock temporal PDF and is truncated at five years in line with Hainzl et al., 2016); and $q$, $D$, and $\gamma$, which are the parameters of the spatial PDF of the aftershock location relative to a parent mainshock with magnitude $m_i$ and location $(x_i, y_i)$. The spatial PDF by Ogata and Zhuang (2006) is used when the rupture geometry is not available (i.e., for events generated by the distributed seismicity module—see Section 2.1.2—or from other aftershocks). The spatial PDF by Guo et al. (2015) is used when the rupture geometry is available (i.e., when the mainshock is simulated by the fault-based model—see Section 2.1.1). Both of these spatial PDFs only consider epicentral distance. Consistent with previous studies (e.g., Papadopoulos et al., 2020), aftershock depths are sampled using the same empirical depth distribution of the distributed seismicity module (see Supporting Information S1 for more details), which can produce depth profiles compatible with the earthquake catalog. For additional details on the ETAS-based formulation implemented in this study, the reader is referred to Iacoletti et al. (2022).

In this study, the Iacoletti et al. (2022) sequence-averaged calibration methodology is explored to parameterize the aftershock simulator. Iacoletti et al. (2022) investigate the challenges of calibrating the ETAS

model for simulation-based PSHA and demonstrate that the sequence-averaged calibration methodology can generate reasonably accurate stochastic event sets (at least for the limited set of case studies considered in that paper). The sequence-averaged calibration methodology is designed to specifically capture the average characteristics of sequences identified by the declustering algorithm (i.e., number of aftershocks, spatial and magnitude-frequency distributions). This is achieved by first detecting all sequences in the non-declustered catalog, fitting several ETAS models on a sequence-by-sequence basis, and then averaging the resulting parameters. The declustering algorithm used to identify sequences in the catalog is the same one used for calibrating the distributed seismicity module (in this study, Gardner & Knopoff, 1974). This ensures that the aftershock simulator is consistent with the mainshock PSHA and only models seismicity removed by the declustering algorithm.

Consistent with Iacoletti et al. (2022), the truncated GR distribution used to model the magnitude of the aftershocks has: (a) minimum magnitude equal to the minimum reference magnitude $m_{\min}$ of the ETAS model; (b) $b$-value calibrated with the sequence-averaged calibration approach; and (c) maximum magnitude equal to min($M_{ms}$, $M_{\max,d}$) in which $M_{ms}$ is the minimum of the mainshock magnitude that generated the aftershocks and $M_{\max,d}$ is the maximum magnitude of the closest point source in the distributed seismicity module. The first limit on the maximum magnitude is justified given that the aftershock simulator only describes aftershock seismicity filtered by the declustering algorithm. The Gardner and Knopoff (1974) declustering algorithm (commonly implemented in practice, e.g., Field et al., 2014), used in this study, is based on the assumption that the mainshock is the event with the highest magnitude in a given sequence. In this context, events in the mainshock stochastic event set are assumed to have the largest magnitude within each cluster, and the aftershock simulator should not produce larger events (otherwise, the aftershock simulator would produce mainshocks). The additional cap on the maximum magnitude is motivated by the fact that very high-magnitude "triggered events" (as defined by Toda et al., 1998) often have complex rupture geometries and are already included in the fault interaction module of the fault-based seismicity module.

The simulation method described by Iacoletti et al. (2022) is used to add the aftershocks to each of the mainshock stochastic event sets generated, as described in Section 2.1.3. Five years of pre-simulation-period seismicity are added to each mainshock stochastic event set to account for the aftershocks due to past seismicity. The aftershock temporal PDF is truncated to neglect the background seismicity component of the classic ETAS formulation. This is because all parent events are assumed to be either known (i.e., part of the previous five years of historical seismicity) or mainshocks generated by the mainshock stochastic event set generator described in Section 2.1 (Field et al., 2017). Please see Iacoletti et al. (2022) for more details.

### 2.3. Ground Motion and Hazard Curves

The $n$th synthetic earthquake catalog contains $K_n$ ruptures (mainshocks and aftershocks). The ground-motion fields for each rupture are simulated by sampling the probability distribution defined by the considered ground-motion models (GMMs). The intra-event residuals are simulated accounting for both spatial correlation and cross-correlation, that is, correlation between different $IM$s (e.g., Huang & Galasso, 2019; Weatherill et al., 2015). The inter-event residuals are sampled independently for each event in the stochastic event set. The site-effects are accounted for using $V_{S30}$ (shear wave velocity in the upper 30 m) values from available sources.

The full set of ground motions simulated for each rupture of the $N_c$ synthetic earthquake catalogs can be used to derive hazard curves. The method described by Iacoletti et al. (2021) (modified from Ebel & Kafka, 1999) is used in this study. The probability that a ground-motion intensity $IM$ exceeds a ground-motion level $iml$ at a given site is computed as:

$$P(IM > iml) = \frac{1}{N_c} \sum_{n=1}^{N_c} I(im, iml) \tag{2}$$

where $im$ is the ground-motion intensity at the specific site associated with a generic rupture and $I(im, iml)$ is an indicator function which returns a value of one if $im > iml$ for at least one rupture in the $n$th catalog, zero otherwise.

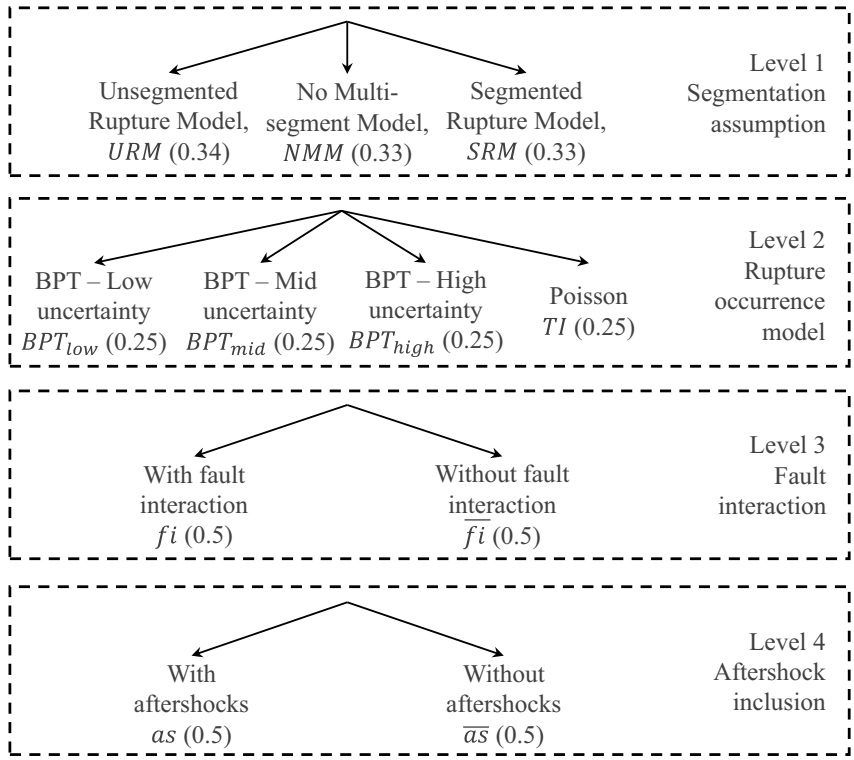


**Figure 3.** Illustration of the logic tree branches for the four levels of epistemic uncertainty investigated. The numbers in parentheses indicate the weights of the corresponding logic-tree branch.

### 2.4. Uncertainties and Sensitivity Analysis

PSHA results are affected by several sources of uncertainty, which are often categorized as aleatoric or epistemic (McGuire, 2004). Epistemic uncertainties in PSHA are typically accounted for using a logic tree approach, in which an individual branch quantifies all aleatoric uncertainties, while the spread of branches describes the epistemic uncertainty (e.g., Bommer & Scherbaum, 2008). The logic tree approach is used herein to investigate the influence of epistemic uncertainty among the proposed framework components that are not typically considered in conventional PSHA approaches: (a) the segmentation assumptions (*URM*; *NMM*; or *SRM*); (b) the rupture occurrence model ($BPT_{mid}$, BPT with mid recurrence uncertainty; $BPT_{high}$, BPT with high recurrence uncertainty; $BPT_{low}$, BPT with low recurrence uncertainty; and *TI*, time-independent); (c) whether the fault interaction process is considered ($fi$) or not ($\overline{fi}$); and (d) whether the aftershocks are included ($as$) or not ($\overline{as}$). A thorough sensitivity study of all sources of epistemic uncertainty in PSHA (e.g., fault geometry information, slip rate data, the earthquake catalog used; see Gerstenberger et al., 2020, for a review of uncertainties in PSHA) is outside the scope of this study. It is acknowledged, however, that the specific uncertainty sources examined here may not be as significant as traditional ones. Each of the considered epistemic uncertainties corresponds to a different level of the logic tree shown in Figure 3. For this study, the weights are uniform at each logic tree level, and 100,000 stochastic event sets are generated for each logic tree branch up to level 3 (for a total of 24 branches). Level 4 adds (or not) aftershocks to the mainshock stochastic event sets, increasing the number of branches to 48.

The logic tree in Figure 3 is used for a variance-based sensitivity analysis (e.g., Saltelli et al., 2010). For a given model of the form $Y = g(\boldsymbol{X})$, variance-based methods are probabilistic sensitivity analyses that quantify the sensitivity of $Y$ to $\boldsymbol{X}$ in terms of a reduction in the variance of $Y$. In this study, $Y$ is the ground-motion intensity for a single *IM* and for a specified return period (RP), the function $g(\cdot)$ represents the implementation of the proposed PSHA framework, and inputs $\boldsymbol{X}$ are the variables related to epistemic uncertainty sources 1–4 (segmentation assumption, rupture occurrence model, fault interaction and aftershock inclusion). Consistent with the methodology in Saltelli et al. (2010), four matrices are generated: (a) $\boldsymbol{A}$, built with 2,000 samples (e.g., Cremen & Baker, 2020) of each of the four input types depicted in the logic tree (according to the uniform distribution at the corresponding level of the tree, see Figure 3); (b) $\boldsymbol{B}$ with an additional 2,000 samples generated in the same way

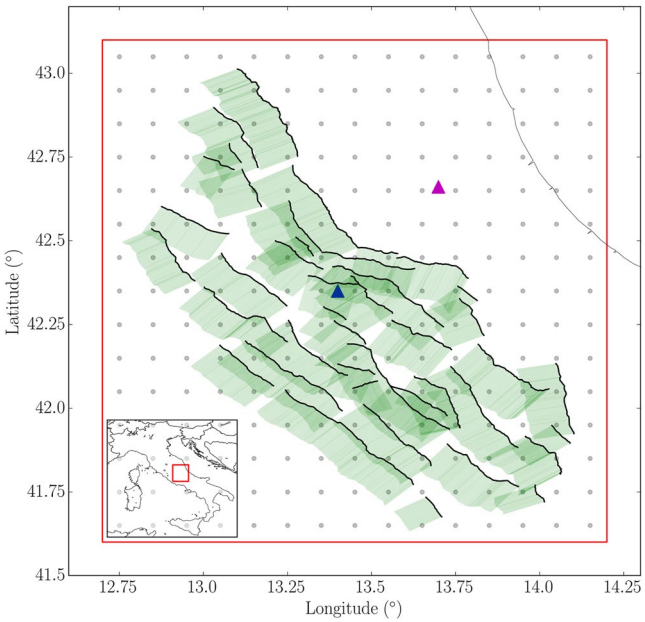


**Figure 4.** Study area, along with the 43 considered fault segments (Scotti et al., 2021). Fault traces are highlighted with a thicker black line and the distributed seismicity grid (from the SHARE seismic hazard model, Woessner et al., 2015) is shown in gray color. The cities of L'Aquila (longitude 13.40°, latitude 42.35°) and Teramo (longitude 13.70°, latitude 42.66°) are marked with blue and magenta triangles, respectively.

as $\boldsymbol{A}$; (c) $\boldsymbol{C}_i$, built by substituting the $i$th column of matrix $\boldsymbol{A}$ for the $i$th column of matrix $\boldsymbol{B}$; and (d) $\boldsymbol{D}_i$, built by substituting the $i$th column of matrix $\boldsymbol{B}$ for the $i$th column of matrix $\boldsymbol{A}$. Each row of each matrix is used to sample 10,000 stochastic events sets and compute the hazard curves as in Section 2.3. For a single $IM$ and a single RP, $Y_A$, $Y_B$, $Y_{C_i}$, and $Y_{D_i}$ are ground-motion intensity vectors corresponding to each row of $\boldsymbol{A}$, $\boldsymbol{B}$, $\boldsymbol{C}_i$, and $\boldsymbol{D}_i$, respectively. The first-order (main) sensitivity coefficient is estimated as:

$$S_i = \frac{\frac{1}{2N}\left(\sum_{j=1}^{N} Y_A^{(j)} Y_{C_i}^{(j)} + \sum_{j=1}^{N} Y_B^{(j)} Y_{D_i}^{(j)}\right) - \hat{f}_0^2}{\frac{1}{2N}\sum_{j=1}^{N}\left[\left(Y_A^{(j)}\right)^2 + \left(Y_B^{(j)}\right)^2\right] - \hat{f}_0^2} \tag{3}$$

where $N = 2{,}000$ is the number of generated samples, $\hat{f}_0^2 = \frac{1}{2N}\sum_{j=1}^{N}\left(Y_A^{(j)} Y_B^{(j)} + Y_{C_i}^{(j)} Y_{D_i}^{(j)}\right)$ per Yun et al. (2017) and $Y_A^{(j)}$, $Y_B^{(j)}$, $Y_{C_i}^{(j)}$, and $Y_{D_i}^{(j)}$ are the $j$th elements of $Y_A$, $Y_B$, $Y_{C_i}$, and $Y_{D_i}$, respectively. For example, an $S_i$ value of 0.2 implies that fixing the value of $i$th input would reduce the variance of $Y$ by 20% on average. More details on variance-based sensitivity analysis can be found in Saltelli et al. (2010).

## 3. Case Study

### 3.1. Mainshock Stochastic Event Set

Central Italy (bounding box of longitudes [12.7°, 14.2°] and latitudes [41.6°, 43.2°]) is selected as a case study to demonstrate the proposed framework (Figure 4). The cities of L'Aquila (longitude 13.40°, latitude 42.35°) and Teramo (longitude 13.70°, latitude 42.66°) are used as target locations for this illustrative application. L'Aquila is selected because a large number of its buildings were damaged during the 2009 Central Italy sequence (e.g., Bazzurro et al., 2009) and because of its close proximity to modeled fault segments (details to follow). Teramo is selected as it is one of the largest urban centers in the study area and is farther away from modeled fault segments than L'Aquila.

#### 3.1.1. Fault-Based Seismicity Module

Figure 4 shows the geometry (fault segment surface and trace) of the 43 considered fault segments (from the Fault2SHA Central Appennines laboratory, Faure Walker et al., 2021; Scotti et al., 2021) and the study area.

The geometries, slip rates and dates of the last event of the considered fault segments are taken from Scotti et al. (2021) and Valentini et al. (2019) (see Table S1 in Supporting Information S1). Slip rates from Valentini et al. (2019) are used where relevant information is missing from Scotti et al. (2021). Consistent with Valentini et al. (2019), the magnitude scaling relationship by Leonard (2010) is used in this study. The calibration of the fault-based seismicity module also includes paleoseismic/historical records, which are available for four locations along the FucinoOvindoliPezza fault (Galli et al., 2008, 2012; Pantosti et al., 1996; Scotti et al., 2021), two locations along the CampoFelice fault (Salvi et al., 2003; Scotti et al., 2021), three locations along the MtVettore fault (Cinti et al., 2019; Scotti et al., 2021), one location along the PaganicaSanDemetrioNeVestini fault (Valentini et al., 2019), and one location along the Sulmona fault (Galli et al., 2014).

#### 3.1.2. Distributed Seismicity Module

The Catalogo Parametrico dei Terremoti Italiani (CPTI15, Rovida et al., 2020b) is used to calibrate the distributed seismicity module (see Data Availability Statement). The CPTI15 catalog combines all known information on significant Italian earthquakes (including macroseismic data) and has been used to develop the latest official hazard study for Italy (Meletti et al., 2021). It comprises 4,703 $M_W \geq 2.2$ events from 1005 to 2019. The procedure described in Section 2.1.2 and Supporting Information S1 is used to calibrate the distributed seismicity module, with a buffer area 1.5° larger than the study area (shown in Figure 5). This ensures a robust estimate of the $b$-value and that the smoothing procedure is not affected by the removal of events outside the study area.

10.1029/2022EA002253

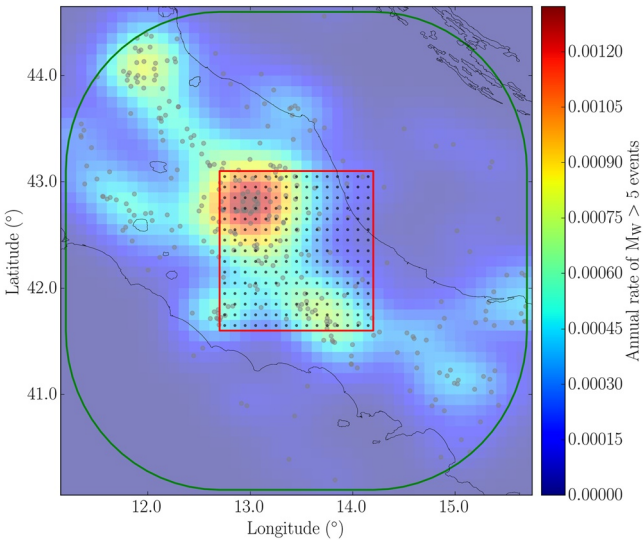


**Figure 5.** Smoothed seismicity rates of events with $M_W > 5$ events. The red polygon is the study area in Figure 4 and the green polygon is the buffer area used to calibrate the distributed seismicity module (black dots). The gray dots show the $M_W > 4.3$ events of the CPTI15 catalog between 1871 and 2020.

Consistent with Frankel (1995), the smoothing procedure uses lower magnitude events (in this study, $M_W > 4.3$ with 1871 as the completeness year, see Supporting Information S1) to infer the rate of $M_W > 5$ earthquakes. The correlation distance is set to $c = 30\ km$ (consistent with Valentini et al., 2019) and the grid of distributed point sources (see Figure 4) is taken from the SHARE seismic hazard model (Woessner et al., 2015). Figure 5 shows the resulting smoothed $M_W > 5$ seismicity, along with the $M_W > 4.3$ events in the catalogs.

The *b*-value of the GR distributions is assumed equal for all the grid points in the study area. This is in line with previous studies that considered Central Italy as a single macro-region for *b*-value estimation (Visini et al., 2022; Woessner et al., 2015). The *b*-value is calculated with the method by Aki (1965) and is equal to 1.05. The maximum magnitudes from the SHARE seismic hazard model (Woessner et al., 2015) are used to compute the GR distribution of each point source. For point sources (i.e., cells) that spatially overlap with fault segments in Figure 4, the final GR distribution is computed as described in Section 2.1.2 and Supporting Information S1. The total smoothed $M_W > 5$ seismicity rate of the distributed seismicity is 0.218; this value for the declustered catalog is 0.228.

To reduce the computational cost of the analyses, a limited number of uneven depth bins are used to compute the empirical depth distribution (i.e., histograms). Table 1 provides the depth distribution of events. The center depth of each bin (or 350 km in the case of events with depth >100 km) is used to generate the ruptures. The focal mechanism distribution for each point source is taken from the SHARE seismic hazard model (Woessner et al., 2015).

### 3.1.3. Combined Mainshock Event Set Generation

100,000 one-year-long stochastic event sets starting from 2022 are generated with the fault-based and the distributed seismicity modules. Table 2 shows the number of generated mainshocks for each of the logic tree branches (Figure 3), along with the average magnitude of the simulated events. The *NMM* analyses (no multi-segment model) generally produce the highest number of events. This is due to the inversion process that distributes similar slip rate (i.e., seismic moment) budgets across fewer ruptures with lower magnitudes (details in Iacoletti et al., 2021). The *SRM* branches produce the lowest number of events because they only incorporate ruptures with entire single fault segments (consistent with the characteristic earthquake model); the number of ruptures is lower, but the average magnitude of the events is higher compared to other analyses. *URM* branches produce a lower number of events with respect to the *NMM* branches, but the average magnitude of the *URM* events is slightly higher because these branches include higher magnitude multi-segment ruptures (excluded in *NMM* branches). The time-independent rupture occurrence model (*TI* branches) produces a higher number of events with a higher average magnitude with respect to the time-dependent branches. This is because the time-dependent models penalize rupture occurrences on fault segments that ruptured in the recent past (e.g., the MtVettore fault ruptured during the 2016 Central Italy sequence).The branches including fault interaction (*fi* branches) generally produce more events than those without fault interaction ($\overline{fi}$ branches). However, this finding cannot be generalized because it depends on the fault geometries and the magnitudes of the considered ruptures (Iacoletti et al., 2021). As expected, the number of mainshocks from the distributed seismicity module is reasonably constant across the branch analyses and consistent with the total distributed rate of events within the study area.

**Table 1**
*Empirical Depth Distribution*

| Depth bin (km) | Center depth (km) | Probability |
|---|---|---|
| (0,10] | 5 | 0.205 |
| (10,14] | 12 | 0.688 |
| (14,26] | 20 | 0.064 |
| (26,40] | 33 | 0.025 |
| (40,100] | 70 | 0.011 |
| >100 | 350 | 0.007 |

Figure 6 compares the MFDs of the stochastic event sets and those of the CPTI15 catalog. The MFDs for the mainshock-only stochastic event set always lie within the 95% confidence interval of the MFD for the declustered CPTI15 catalog, up to its maximum sampled magnitude. This comparison is consistent with the findings of Valentini et al. (2019). The non-declustered CPTI15 catalog contains around 20% more $M_W > 5$ events than the stochastic event sets (mostly $5 < M_W < 5.5$ events). This is probably because the stochastic event sets do not

**Table 2**
*Number of Generated $M_W \geq 5$ Events From the Mainshock Stochastic Event Set Generator and the Aftershock Simulator for Each Branch of the Logic Tree (Figure 3)*

| Logic tree branch | Mainshocks from fault-based seismicity module | Mainshocks from distributed seismicity module | Total number of mainshocks | Total number of aftershocks |
|---|---|---|---|---|
| *URM-BPT$_{mid}$-fi* | 999 (6.65) | 21,689 (5.39) | 23,688 | 12,082 (5.33) |
| *URM-BPT$_{mid}$-$\overline{fi}$* | 936 (6.67) | 21,993 (5.38) | 23,929 | 12,025 (5.33) |
| *URM-BPT$_{high}$-fi* | 1,011 (6.68) | 21,832 (5.39) | 23,843 | 12,517 (5.33) |
| *URM-BPT$_{high}$-$\overline{fi}$* | 1,019 (6.69) | 21,994 (5.39) | 24,013 | 12,935 (5.34) |
| *URM-BPT$_{low}$-fi* | 912 (6.68) | 21,705 (5.39) | 23,617 | 11,777 (5.33) |
| *URM-BPT$_{low}$-$\overline{fi}$* | 884 (6.67) | 21,662 (5.39) | 23,546 | 11,015 (5.33) |
| *URM-TI-fi* | 1,126 (6.71) | 21,732 (5.39) | 23,858 | 13,392 (5.34) |
| *URM-TI-$\overline{fi}$* | 1,107 (6.72) | 21,811 (5.39) | 23,918 | 13,209 (5.34) |
| *NMM-BPT$_{mid}$-fi* | 1,085 (6.64) | 21,771 (5.39) | 23,856 | 11,662 (5.33) |
| *NMM-BPT$_{mid}$-$\overline{fi}$* | 1,066 (6.65) | 21,898 (5.39) | 23,964 | 11,922 (5.33) |
| *NMM-BPT$_{high}$-fi* | 1,145 (6.64) | 21,802 (5.39) | 23,947 | 12,209 (5.33) |
| *NMM-BPT$_{high}$-$\overline{fi}$* | 1,029 (6.65) | 21,600 (5.39) | 23,629 | 11,627 (5.33) |
| *NMM-BPT$_{low}$-fi* | 1,033 (6.64) | 21,811 (5.39) | 23,844 | 11,554 (5.34) |
| *NMM-BPT$_{low}$-$\overline{fi}$* | 1,082 (6.64) | 21,945 (5.39) | 24,027 | 12,077 (5.34) |
| *NMM-TI-fi* | 1,200 (6.66) | 21,547 (5.39) | 23,747 | 12,218 (5.32) |
| *NMM-TI-$\overline{fi}$* | 1,158 (6.65) | 21,785 (5.39) | 23,943 | 11,910 (5.32) |
| *SRM-BPT$_{mid}$-fi* | 669 (6.75) | 21,882 (5.39) | 23,551 | 10,523 (5.33) |
| *SRM-BPT$_{mid}$-$\overline{fi}$* | 679 (6.76) | 21,994 (5.39) | 23,673 | 10,793 (5.32) |
| *SRM-BPT$_{high}$-fi* | 683 (6.76) | 21,378 (5.39) | 23,061 | 10,421 (5.33) |
| *SRM-BPT$_{high}$-$\overline{fi}$* | 700 (6.76) | 21,829 (5.39) | 23,529 | 10,779 (5.33) |
| *SRM-BPT$_{low}$-fi* | 707 (6.76) | 21,557 (5.38) | 23,264 | 10,745 (5.33) |
| *SRM-BPT$_{low}$-$\overline{fi}$* | 679 (6.76) | 21,821 (5.39) | 23,500 | 10,756 (5.33) |
| *SRM-TI-fi* | 966 (6.72) | 21,888 (5.39) | 23,854 | 11,815 (5.33) |
| *SRM-TI-$\overline{fi}$* | 906 (6.73) | 21,980 (5.39) | 23,886 | 11,845 (5.33) |

*Note.* The average magnitude $M_W$ of the events is reported in parenthesis.

include aftershocks $5 < M_W < 5.5$ of mainshocks occurring outside the study area (see Figure 4), which could lead to a general underestimation of hazard within the study area. However, the hazard estimates at both target locations (L'Aquila and Teramo) should only be marginally affected by this simplification, given their location well within the bounds of the study area, at far distances from the excluded events. For this reason, the stochastic event sets in this study are considered acceptable. It is worth noting that other studies based on classical ETAS approaches also seem to provide a good description of the Italian seismicity, especially in the $5 < M_W < 5.5$ range (e.g., Šipčić et al., 2022).

### 3.2. Aftershock Simulation Methodology

The Homogenized Instrumental Seismic Catalog (HORUS, Lolli et al., 2020a) is used to calibrate the parameters of the ETAS-based aftershock simulator (see Data Availability Statement). The HORUS catalog focuses on instrumental Italian seismicity and comprises 88,517 $M_W \geq 2$ events from 3 January 1960 to 31 December 2020. The HORUS catalog is preferred to CPTI15 for the calibration of the parameters of the aftershock simulator because: (a) it only accounts for instrumental seismicity, which means that all magnitude and spatial location values are reasonably reliable; and (b) it includes a larger number of lower magnitude events (i.e., it has a lower magnitude of completeness), which is important for the sequence-averaged calibration approach. According to the Stepp (1972) method, the HORUS catalog appears to be complete for $M_W \geq 3$ from 1980.

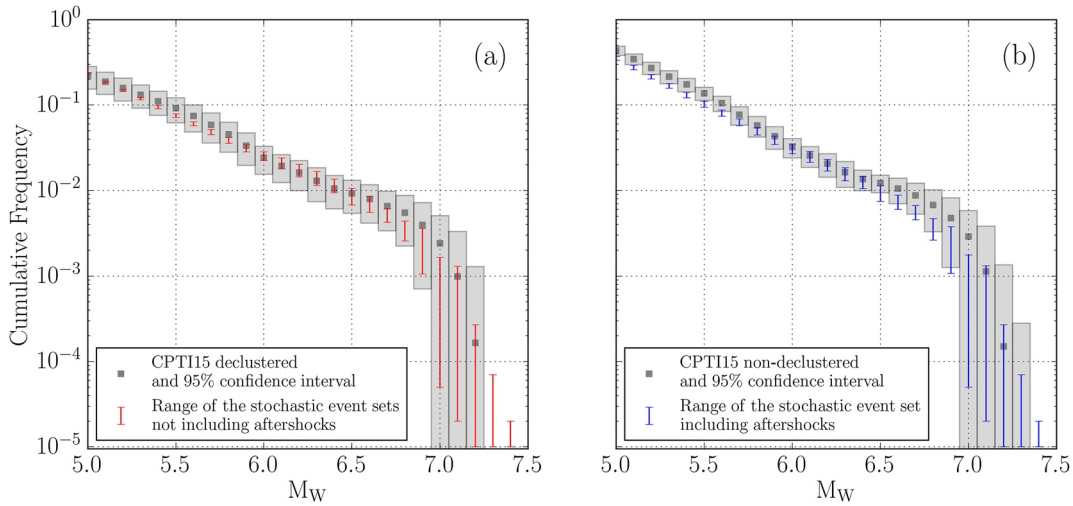


**Figure 6.** Comparison between the MFDs of the: (a) mainshock-only; and (b) mainshock and aftershock stochastic event sets, with the: (a) declustered, and (b) non-declustered MFDs of the CPTI15 catalog (based the completeness periods reported by Scotti et al., 2021). The gray patches are the 95% confidence intervals of the cumulative frequency, calculated per Scotti et al. (2021).

Table 3 reports the parameters of the ETAS-based aftershock simulator for Italy calibrated with the sequence-averaged approach by Iacoletti et al. (2022) for $m_{\min} = 3$ and using available finite fault models (see Data Availability Statement). Each of the mainshock stochastic event sets is updated with five years of $M_W \geq 3$ seismicity (493 events) between 2017 (included) and 2022 (excluded). To be consistent with the calibration, the aftershock simulations are carried out for $M_W \geq 3$. The final catalogs are then filtered for a minimum magnitude of $M_W$ 5, in line with the mainshock stochastic event set.

Table 2 also shows the number of generated aftershocks for the 24 logic tree branches (Figure 3) that include aftershock generation. On average, more aftershocks are generated for analyses with a higher number of mainshocks (e.g., *NMM* vs. *SRM* branches).

### 3.3. Hazard Curves and Maps

For each event in the stochastic event sets, ground-motion estimates are computed using the GMM developed by Cauzzi et al. (2015). Lanzano et al. (2020) evaluated several GMMs based on Italian active shallow crustal earthquakes (including events that occurred in Central Italy) and selected Cauzzi et al. (2015) as one of the best performing GMMs. In this study, Cauzzi et al. (2015) is preferred to other well-performing GMMs in Lanzano et al. (2020) because it uses rupture distance as the distance metric, which is particularly useful when the geometry of the rupture is available (for the fault-based seismicity module). The intra-event residuals are simulated with the procedure proposed by Markhvida et al. (2018). Markhvida et al. (2018)'s procedure is not necessarily appropriate for all areas of the world, but it has been applied in different regions, such as China (You et al., 2021) and Chile (Ceferino et al., 2020). The magnitude, faulting characteristics (e.g., dip, rake angles), and source-to-site distance measures are evaluated on a rupture-by-rupture case. $V_{S30}$ values are taken from the map by Mori et al. (2020).

Figure 7 shows the effect of aftershock inclusion on the hazard map for PGA with RP = 475 years. Figure 7 shows the hazard map for $URM\text{-}BPT_{mid}\text{-}fi\text{-}\overline{as}$ (top panel) and the ratio $r_a = URM\text{-}BPT_{mid}\text{-}fi\text{-}as/URM\text{-}BPT_{mid}\text{-}fi\text{-}\overline{as}$ (bottom panel). Figure 7 (top panel) demonstrates that $URM\text{-}BPT_{mid}\text{-}fi\text{-}\overline{as}$ provides higher PGA values in the North-West portion of the study area. The bottom panel shows that including aftershocks amplifies the PGA values as expected (i.e., the ratio $r_a$ is always greater than 1). The bottom panel also highlights the fact that $r_a$ is not uniformly distributed in space (this finding is also valid for other segmentation assumptions).

**Table 3**
*Sequence-Averaged Calibrated ETAS-Based Aftershock Simulator Used in This Study (Iacoletti et al., 2022)*

| $A$ | $\alpha$ | $c$ | $p$ | $D$ | $q$ | $\gamma$ | $b$ |
|---|---|---|---|---|---|---|---|
| 0.301 | 1.56 | 0.6E−02 | 1.23 | 8.5E−04 | 2.30 | 0.94 | 1.0 |

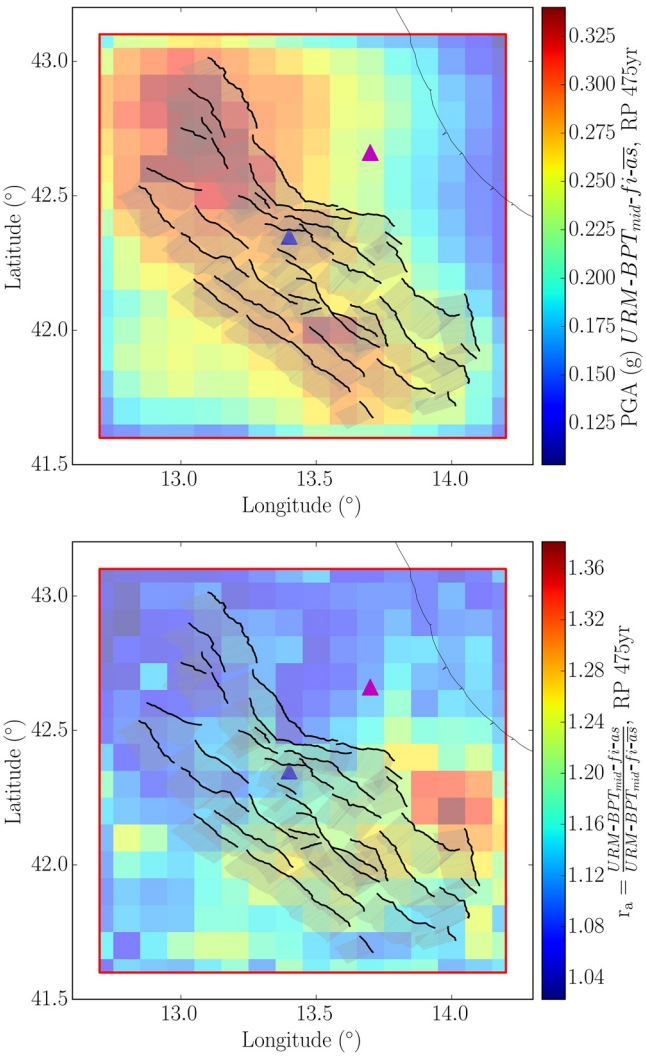


**Figure 7.** Hazard map for PGA with a return period of 475 years for branch *URM-BPT*$_{mid}$*-fi-*$\overline{as}$ (top panel) and the ratio $r_a$ = *URM-BPT*$_{mid}$*-fi-as*/*URM-BPT*$_{mid}$*-fi-*$\overline{as}$ (bottom panel). See Figure 3 for the corresponding branch explanations. L'Aquila and Teramo are marked with blue and magenta triangles, respectively.

Figure 8 is similar to Figure 7 but compares the simplest branch (*SRM-TI-*$\overline{fi}$*-*$\overline{as}$) with one of the most complex ones (*URM-BPT*$_{mid}$*-fi-as*). Figure 8 (top panel) shows that the simplest branch provides higher PGA values in the area around L'Aquila. Compared to the simplest analysis (ratio $r_c$ = *URM-BPT*$_{mid}$*-fi-as*/*SRM-TI-*$\overline{fi}$*-*$\overline{as}$ in the bottom panel of Figure 8), the complex branch provides lower PGA values around L'Aquila. These results for L'Aquila are broadly consistent with a time-dependent interpretation of seismicity: the fault contributing the most to the hazard at L'Aquila (i.e., the Paganica fault) has recently ruptured (i.e., 2009 L'Aquila earthquake) and is therefore at a very early stage of the earthquake cycle (e.g., Pace et al., 2016). This means that the hazard at L'Aquila is expected to be lower than average. Time-independent occurrence models included in the simplest branch cannot capture this phenomenon, leading to higher hazard values than time-dependent ones.

Figure 9 displays the PGA hazard curves at L'Aquila and Teramo for the logic tree branches shown in Figures 7 and 8 (i.e., *SRM-TI-*$\overline{fi}$*-*$\overline{as}$, *URM-BPT*$_{mid}$*-fi-as* and *URM-BPT*$_{mid}$*-fi-*$\overline{as}$) and the range of variability across all 48 branches. Figure 9 also shows the ratio (for specific annual probabilities of exceedance) of the *URM-BPT*$_{mid}$*-fi-as* and *URM-BPT*$_{mid}$*-fi-*$\overline{as}$ hazard curves with respect to that of *SRM-TI-*$\overline{fi}$*-*$\overline{as}$. Figures S1–S3 in Supporting Information S1 show the equivalent hazard curves in Figure 9 for SA (spectral acceleration) at 0.2, 0.5, and 1s. The top row of Figure 9 for L'Aquila shows that *SRM-TI-*$\overline{fi}$*-*$\overline{as}$ produces higher ground-motion amplitudes than *URM-BPT*$_{mid}$*-fi-as* for annual probabilities of exceedance lower than around 0.02 (RP higher than 50 years) and that the corresponding ratio ranges from 0.50 to 1.25. The bottom row of Figure 9 shows that at Teramo the hazard-curve ratios range from 0.80 to 1.25. The range of hazard-curve variability at Teramo is visibly lower than that at L'Aquila. Similar findings can be observed in Figures S1–S3 of Supporting Information S1. Figure 9 also shows that including aftershocks (*URM-BPT*$_{mid}$*-fi-as* vs. *URM-BPT*$_{mid}$*-fi-*$\overline{as}$) increases the ground-motion estimates between 2% and 35%.

### 3.4. Uncertainties and Sensitivity Analysis

The cities of L'Aquila and Teramo (see Figure 4) are used to carry out sensitivity analyses in this section. Figure 10 shows the $S_i$ values for PGA and RPs of 50, 200 and 475 years. Similar sensitivity results for SA at 0.2, 0.5 and 1s are provided in Figures S4–S6 of Supporting Information S1.

The $S_i$ values for fault interaction are low for both cities and all RPs. This is because the event occurrence probability is less sensitive to the inclusion or not of fault interaction than the choice of rupture occurrence model in this case study (e.g., Iacoletti et al., 2021; Murru et al., 2016). At L'Aquila, aftershock inclusion has the highest $S_i$ for RP = 50 years, while the rupture occurrence model has the highest $S_i$ for RP = 200 years and RP = 475 years. Similar findings can be observed in Figures S4–S6 of Supporting Information S1. The segmentation assumption has the second highest $S_i$ for RP = 50 years. At Teramo, aftershock inclusion has the highest $S_i$ for all RPs (except RP = 475 years), and fault-related input variables become much less relevant. The sensitivity of the ground-motion estimates to aftershock inclusion generally decreases: (a) with increasing RPs; and (b) for SA at periods greater than 0.2s (see Figure S5 and S6 in Supporting Information S1).

## 4. Discussion

Figure 9 highlights the consequences of increasing the complexity of modeling assumptions. For sites near the fault segments included in the fault-based seismicity module (e.g., at L'Aquila), choosing *URM-BPT*$_{mid}$*-fi-as*

10.1029/2022EA002253

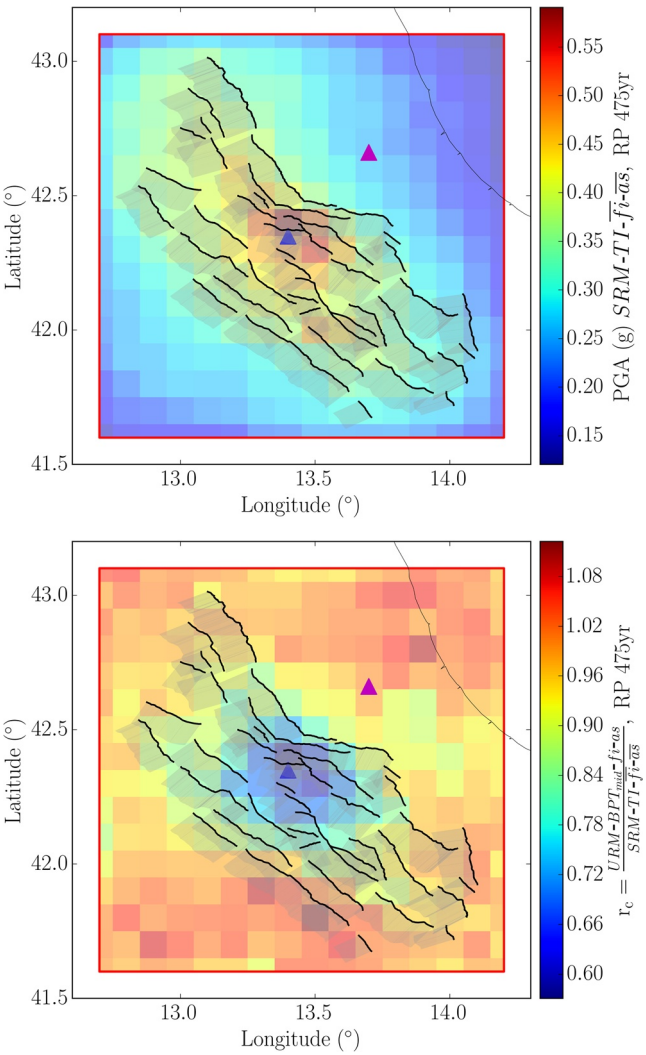


**Figure 8.** Hazard map for PGA with a return period of 475 years for branch *SRM-TI-$\overline{fi}$-$\overline{as}$* (top panel) and the ratio $r_c$ = *URM-BPT$_{mid}$-fi-as/SRM-TI-$\overline{fi}$-$\overline{as}$* (bottom panel). See Figure 3 for the corresponding branch explanations. L'Aquila and Teramo are marked with blue and magenta triangles, respectively.

over *SRM-TI-$\overline{fi}$-$\overline{as}$* increases the ground-motion amplitudes for high annual probabilities of exceedance (as much as 25%) and significantly decreases the ground-motion amplitudes for low annual probabilities of exceedance (as much as 50%). Figure 8 also confirms that at L'Aquila and surrounding areas, *URM-BPT$_{mid}$-fi-as* provides ground-motion amplitudes around 40% less than those of *SRM-TI-$\overline{fi}$-$\overline{as}$* for RP = 475 years. Fault-segment information (e.g., fault traces, slip rate estimates) is not available near Teramo, so was not included in the fault-based seismicity module. As a consequence, the effects of more complex fault modeling is lower at Teramo than at L'Aquila. This finding should encourage future efforts in collecting and storing data for faults close to strategic and important cities, to take full advantage of more complex state-of-the-art methodologies in the field of fault-based PSHA.

The inclusion of aftershocks increases the seismic hazard at all investigated RPs (Figures 7 and 9), which is consistent with other studies (e.g., Iervolino et al., 2014; Papadopoulos et al., 2020). This finding is not surprising, since the aftershock simulator generates a relatively large number of events with average magnitudes comparable to those of the distributed seismicity mainshocks (Table 2). The uneven spatial distribution of aftershocks (which tend to cluster around large magnitude events from the fault-based seismicity module) can cause modest (5%) to severe (40%) increases in the ground-motion estimates, depending on the considered site (see Figure 7).

The results of the sensitivity analyses (Figure 10) highlight the low sensitivity of the hazard estimates to fault interaction. However, this result cannot be generalized (Iacoletti et al., 2021), because fault interaction is strongly dependent on the fault geometry, location and magnitude of events (e.g., Iacoletti et al., 2022b). $S_i$ values for aftershock inclusion are higher for lower RPs. This is because the aftershock simulator generates a substantial number of lower magnitude events in the synthetic catalogs (see Table 2 and Figure 6), which are the largest contributors to the hazard at lower RPs.

At L'Aquila (which lies on three fault segments, i.e., 0 km distance from the surface projection of the faults), fault-related input variables (i.e., the segmentation assumption and the rupture occurrence model) are mainly responsible for the variance of the hazard estimates (see Figure 10). This is because it is less likely that aftershocks will produce ground-motion estimates higher than those of the mainshocks from the fault-based seismicity module (which are generally larger than the mainshocks from the distributed seismicity module, see Table 2). The relative influence of the segmentation assumption decreases compared to that of the rupture occurrence model, for increasing RP. This is because larger magnitude events (which are accounted for across all segmentation models) are the biggest contributors to the hazard for higher RPs (e.g., 200 and 475 years), making the segmentation assumption less relevant than at lower RPs, at least for the considered case study.

At Teramo (i.e., around 25 km away from the surface projection of the closest modeled fault), the influence of fault-based mainshocks on the ground-motion estimates is lower than at l'Aquila, and aftershocks are more likely to produce higher ground-motion intensities relative to those produced by the mainshocks. This is because, even though large mainshocks are less frequently located close to Teramo compared to L'Aquila, relatively large aftershocks can still be generated near Teramo. A similar spatial trend was observed in the 2010–2012 Canterbury sequence (New Zealand), affecting Christchurch: the $M_W$7.2 2010 Darfield mainshock was generated by a major fault (the Darfield fault), around 40 km west of Christchurch. The aftershocks of the Darfield event were generally closer to Christchurch and caused higher ground-motion intensities. Results of the sensitivity analyses indicate that the seismic hazard at Teramo is generally less affected by fault-related input variables (i.e., segmentation assumption, rupture occurrence model and fault interaction) than the hazard at l'Aquila; this observation is also reflected in the smaller range of hazard curve variability associated with Teramo than with

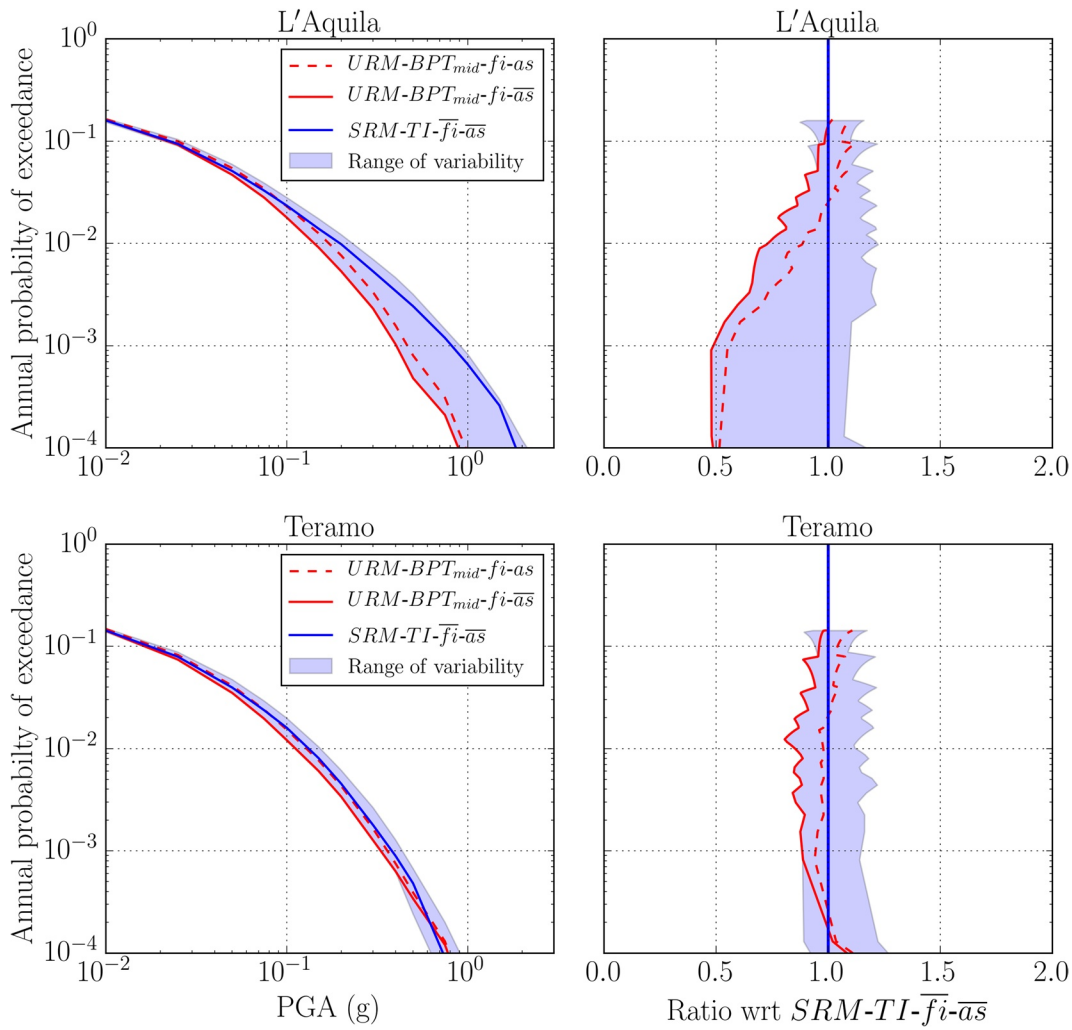


**Figure 9.** Left panels: PGA (peak ground acceleration) hazard curves at L'Aquila (top row) and Teramo (bottom row) for *SRM-TI-$\overline{fi}$-$\overline{as}$*, *URM-BPT$_{mid}$-fi-as* and *URM-BPT$_{mid}$-fi-$\overline{as}$*, including the range of variability across all 48 branches. Right panels: ratios of the hazard curves—with respect to *SRM-TI-$\overline{fi}$-$\overline{as}$*—for *URM-BPT$_{mid}$-fi-as*, *URM-BPT$_{mid}$-fi-$\overline{as}$*, including the range of variability across all 48 branches. See Figure 3 for the corresponding branch explanations.

L'Aquila in Figure 9. Discrepancies between the site's distance to the fault system can be used to explain this finding.

The sensitivity to aftershock inclusion is highest for SA at 0.2s, and decreases for periods of 0.5 and 1.0s. This can be explained by calculating the probability, denoted as $P\left(IM_{M_{low}} > IM_{M_{large}}\right)$, that a lower magnitude event (e.g., $M_W$5.3) exceeds the ground motion produced by a larger magnitude event (e.g., $M_W$6.7) using the GMM developed by Cauzzi et al. (2015). This probability is higher for SA at 0.2s than for PGA, and decreases for SA at 0.5 and 1.0s. This and the fact that aftershocks are mostly low magnitude events (Table 2) can explain why aftershock inclusion has a limited effect on the hazard for SA at 0.5 and 1.0s (see Figures S2, S3, S5, and S6 in Supporting Information S1). The sensitivity results for aftershock inclusion depend on the chosen GMM, because other GMMs will produce different trends in $P\left(IM_{M_{low}} > IM_{M_{large}}\right)$ versus SA. However, a thorough exploration of the sensitivity of the seismic hazard to the adopted GMM is outside the scope of this work.

## 5. Conclusions

This study extends the simulation-based framework in Iacoletti et al. (2021) by: (a) incorporating a distributed seismicity model; and (b) adding aftershocks in the stochastic event sets, using an ETAS-based aftershock

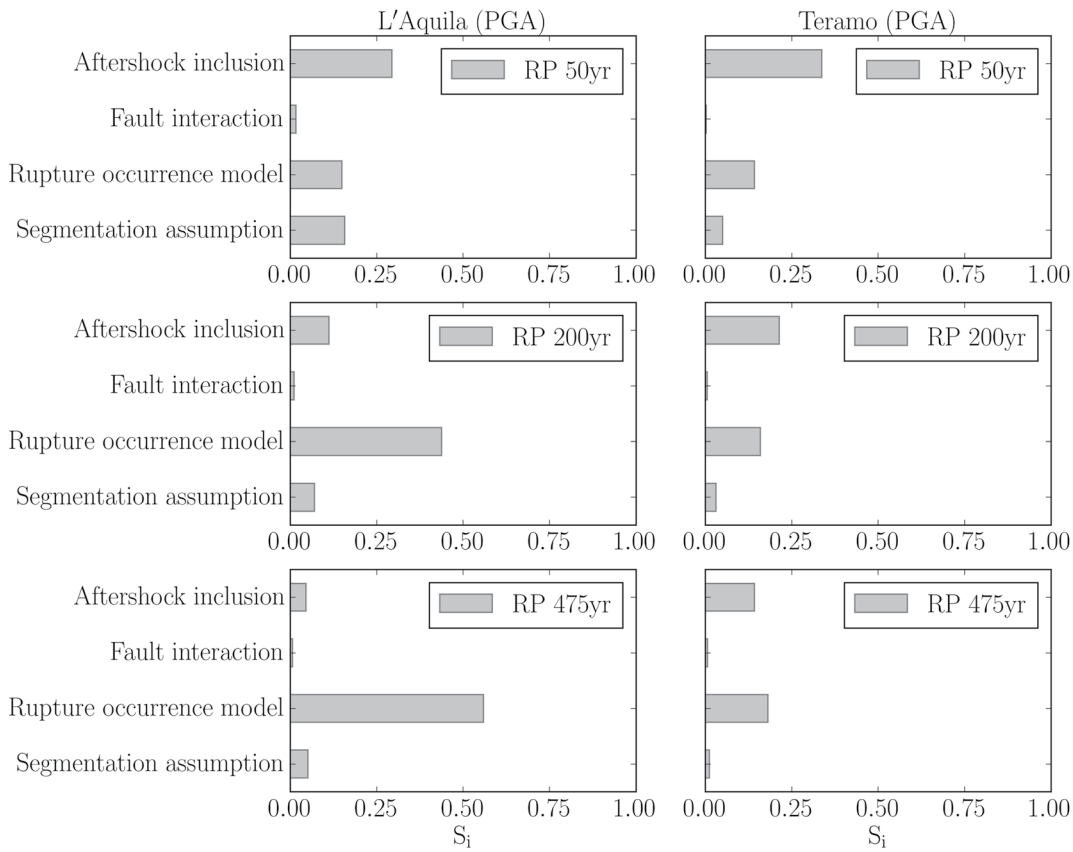


**Figure 10.** Variance-based sensitivity analyses for PGA (RP 50, 200 and 475 years) at L'Aquila (longitude 13.40°, latitude 42.35°) and Teramo (longitude 13.70°, latitude 42.66°).

simulator consistent with the findings of Iacoletti et al. (2022). In doing so, the work proposes a comprehensive end-to-end framework for PSHA that accounts for both long- and short-term time dependencies, addressing the shortcomings of many previously developed approaches for seismic hazard assessment.

The Central Italy region (including the fault segments of Scotti et al., 2021) is used as a case study for demonstrating the integrated framework. It was found that in areas located close to modeled faults (e.g., L'Aquila), increasing the PSHA model complexity with respect to a simplified conventional approach (i.e., that uses a segmented fault model, a time-independent rupture occurrence model, and neglects both fault interaction and aftershock occurrence) can: (a) increase the ground-motion amplitudes for RP lower than 50 years up to 25%; and (b) decrease the ground-motion amplitudes for RP higher than 50 years up to 50%. Although these findings are specific to the selected case study, they should encourage future efforts in collecting fault data close to strategic urban areas to take full advantage of more complex state-of-the-art methodologies in the field of fault-based PSHA. This would be particularly important for matters relating to the solvency capital requirement in the reinsurance industry (commonly set at 200 years RP economic losses; Mitchell-Wallace, 2017) or to values of design ground motion used in Life Safety Limit State requirements (generally around a 475-year RP ground-motion amplitude, e.g., EN, 1998-1, 2004). The inclusion of aftershocks in the analysis always increases the seismic hazard, underlining the importance of considering these events in PSHA studies. For instance, the level of PGA (RP = 475 years) increase that results from aftershock inclusion strongly depends on the site of interest and varies between 5% and 40% for the considered case study.

This study also investigated the sensitivity of the hazard estimates (for PGA, SA at 0.2, 0.5, and 1.0 s) to the following PSHA input variations: (a) the segmentation assumptions used; (b) the long-term rupture occurrence model used; (c) the inclusion (or not) of interaction amongst faults; and (d) the inclusion (or not) of aftershock hazard. The sensitivity results presented in this study are highly dependent on the fault system geometry, the fault data and the GMM used. However, the following conclusions can be drawn:

1. Close to modeled faults and for high RPs (e.g., RP = 200 years and RP = 475 years), the sensitivity of the hazard estimates to the inclusion of aftershocks is generally low. In turn, the fault-related input variables (e.g., rupture occurrence model for the considered case study) greatly affect the variance of the results;
2. Close to modeled faults, the influence of aftershock inclusion on seismic hazard estimates is generally higher for lower RPs (e.g., RP = 50 years) than for higher values;
3. The variance of the results due to aftershock inclusion is lower at near-fault sites than in other areas;
4. Fault interaction has a small effect on the variance of the hazard estimates compared to other analysis inputs.

In general, sensitivity analyses should guide analysts toward trimming the epistemic uncertainty logic tree and reducing computational effort in their PSHA work, without significantly changing the resulting hazard estimates (Porter et al., 2017). The site (and RP) dependency of the sensitivity results for hazard estimates makes it somewhat difficult to generalize conclusions. For example, it can be stated that for a site-specific hazard study at L'Aquila and for RP = 200 years, fault modeling affects the results more than the inclusion of aftershocks. The same statement, however, is false for other sites in Central Italy. For this reason, in future studies, sensitivity analyses should be performed in terms of economic loss metrics (e.g., Porter et al., 2017), which also account for exposure data and provide results that are generally applicable to a broad area (Mitchell-Wallace, 2017).

## Data Availability Statement

The HORUS catalog is available at Lolli et al. (2020b), last accessed 5 October 2021 (Lolli et al., 2020a). The CPTI15 (Catalogo Parametrico dei Terremoti Italiani) catalog is available at Rovida et al. (2020a), last accessed 5 October 2021 (Rovida et al., 2020b). Finite fault models for Italy are available at http://equake-rc.info/srcmod/ (Mai & Thingbaijam, 2014), last accessed 5 October 2021.

**Acknowledgments**
We thank Dr Vincenzo Convertito and an anonymous reviewer for the insightful comments, which helped improve the quality of this manuscript. Salvatore Iacoletti was supported by the UK Engineering and Physical Sciences Research Council (EPSRC), Industrial Cooperative Awards in Science & Technology (CASE) grant (Project reference: 2261161) for University College London and Willis Towers Watson (WTW), through the Willis Research Network (WRN). Gemma Cremen and Carmine Galasso are supported by the European Union's Horizon 2020 research and innovation programme under grant agreement No 821046, project TURNkey (Towards more Earthquake-resilient Urban Societies through a Multi-sensor-based Information System enabling Earthquake Forecasting, Early Warning and Rapid Response actions). Input to and feedback on the study by Dr Crescenzo Petrone, Dr Umberto Tomassetti, and Dr Myrto Papaspiliou (WRN) is greatly appreciated.

## References

Aki, K. (1965). Maximum likelihood estimate of b in the formula logN=a−bM and its confidence limits. *Bulletin of the Earthquake Research Institute Tokyo University*, *43*, 237–239.

Akinci, A., Galadini, F., Pantosti, D., Petersen, M., Malagnini, L., & Perkins, D. (2009). Effect of time dependence on probabilistic seismic-hazard maps and deaggregation for the central Apennines, Italy. *Bulletin of the Seismological Society of America*, *99*(2A), 585–610. https://doi.org/10.1785/0120080053

Bazzurro, P., Alexander, D., Clemente, P., Comerio, M., Sortis, A. D., Filippou, F., et al. (2009). The Mw 6.3 Abruzzo, Italy, earthquake of April 6, 2009. Learning from earthquakes, EERI Special Earthquake Report.

Bommer, J. J., & Scherbaum, F. (2008). The use and misuse of logic trees in probabilistic seismic hazard analysis. *Earthquake Spectra*, *24*(4), 997–1009. https://doi.org/10.1193/1.2977755

Boyd, O. S. (2012). Including foreshocks and aftershocks in time-independent probabilistic seismic-hazard analyses. *Bulletin of the Seismological Society of America*, *102*(3), 909–917. https://doi.org/10.1785/0120110008

Cauzzi, C., Faccioli, E., Vanini, M., & Bianchini, A. (2015). Updated predictive equations for broadband (0.01–10 s) horizontal response spectra and peak ground motions, based on a global dataset of digital acceleration records. *Bulletin of Earthquake Engineering*, *13*(6), 1587–1612. https://doi.org/10.1007/s10518-014-9685-y

Ceferino, L., Mitrani-Reiser, J., Kiremidjian, A., Deierlein, G., & Bambarén, C. (2020). Effective plans for hospital system response to earthquake emergencies. *Nature Communications*, *11*(1), 4325. https://doi.org/10.1038/s41467-020-18072-w

Cinti, F. R., De Martini, P. M., Martini, P. M., Pantosti, D., Baize, S., Smedile, A., et al. (2019). 22-kyr-Long record of surface faulting along the source of the 30 October 2016 earthquake (central Apennines, Italy), from integrated paleoseismic data sets. *Journal of Geophysical Research: Solid Earth*, *124*(8), 9021–9048. https://doi.org/10.1029/2019JB017757

Convertito, V., & Faenza, L. (2014). Earthquake recurrence. In M. Beer, I. A. Kougioumtzoglou, E. Patelli, & I. S.-K. Au (Eds.), *Encyclopedia of earthquake engineering* (pp. 1–21). Springer Berlin Heidelberg. https://doi.org/10.1007/978-3-642-36197-5_236-1

Cremen, G., & Baker, J. W. (2020). Variance-based sensitivity analyses and uncertainty quantification for FEMA P-58 consequence predictions. *Earthquake Engineering & Structural Dynamics*, *50*(3), 811–830. https://doi.org/10.1002/eqe.3370

Ebel, J. E., & Kafka, A. L. (1999). A Monte Carlo approach to seismic hazard analysis. *Bulletin of the Seismological Society of America*, *89*(4), 854–866. https://doi.org/10.1785/bssa0890040854

EN 1998-1. (2004). *Eurocode 8: Design of structures for earthquake resistance—Part 1: General rules, seismic actions and rules for buildings*. CEN.

Faure Walker, J., Boncio, P., Pace, B., Roberts, G., Benedetti, L., Scotti, O., et al. (2021). Fault2SHA central Apennines database and structuring active fault data for seismic hazard assessment. *Scientific Data*, *8*(1), 87. https://doi.org/10.1038/s41597-021-00868-0

Field, E. H. (2015). Computing elastic-rebound-motivated earthquake probabilities in unsegmented fault models: A new methodology supported by physics-based simulators. *Bulletin of the Seismological Society of America*, *105*(2A), 544–559. https://doi.org/10.1785/0120140094

Field, E. H., Arrowsmith, R. J., Biasi, G. P., Bird, P., Dawson, T. E., Felzer, K. R., et al. (2014). Uniform California earthquake rupture forecast, version 3 (UCERF3)–The time-independent model. *Bulletin of the Seismological Society of America*, *104*(3), 1122–1180. https://doi.org/10.1785/0120130164

Field, E. H., Biasi, G. P., Bird, P., Dawson, T. E., Felzer, K. R., Jackson, D. D., et al. (2015). Long-term time-dependent probabilities for the third Uniform California Earthquake Rupture Forecast (UCERF3). *Bulletin of the Seismological Society of America*, *105*(2A), 511–543. https://doi.org/10.1785/0120140093

Field, E. H., Milner, K. R., Hardebeck, J. L., Page, M. T., van der Elst, N., Jordan, T. H., et al. (2017). A spatiotemporal clustering model for the third Uniform California Earthquake Rupture Forecast (UCERF3-ETAS): Toward an operational earthquake forecast. *Bulletin of the Seismological Society of America*, *107*(3), 1049–1081. https://doi.org/10.1785/0120160173

Frankel, A. (1995). Mapping seismic hazard in the central and eastern United States. *Seismological Research Letters*, *66*(4), 14–21. https://doi.org/10.1785/gssrl.66.4.8

Galli, P., Galadini, F., & Pantosti, D. (2008). Twenty years of paleoseismology in Italy. *Earth-Science Reviews*, *88*(1), 89–117. https://doi.org/10.1016/j.earscirev.2008.01.001

Galli, P., Giaccio, B., Peronace, E., & Messina, P. (2014). Holocene paleoearthquakes and early–late pleistocene slip rate on the Sulmona fault (central Apeninnes, Italy). *Bulletin of the Seismological Society of America*, *105*(1), 1–13. https://doi.org/10.1785/0120140029

Galli, P., Messina, P., Giaccio, B., Peronace, E., & Quadrio, B. (2012). Early Pleistocene to late Holocene activity of the Magnola fault (Fucino fault system, central Italy). *Bollettino di Geofisica Teorica ed Applicata*, *53*, 435–458. https://doi.org/10.4430/bgta0054

Gardner, J. K., & Knopoff, L. (1974). Is the sequence of earthquakes in Southern California, with aftershocks removed, Poissonian? *Bulletin of the Seismological Society of America*, *64*(5), 1363–1367. https://doi.org/10.1785/bssa0640051363

Gentile, R., & Galasso, C. (2021). Hysteretic energy-based state-dependent fragility for ground-motion sequences. *Earthquake Engineering & Structural Dynamics*, *50*(4), 1187–1203. https://doi.org/10.1002/eqe.3387

Gerstenberger, M. C., Marzocchi, W., Allen, T., Pagani, M., Adams, J., Danciu, L., et al. (2020). Probabilistic seismic hazard analysis at regional and National scales: State of the art and future challenges. *Reviews of Geophysics*, *49*(2). https://doi.org/10.1029/2019rg000653

Guo, Y., Zhuang, J., & Zhou, S. (2015). An improved space-time ETAS model for inverting the rupture geometry from seismicity triggering. *Journal of Geophysical Research: Solid Earth*, *120*(5), 3309–3323. https://doi.org/10.1002/2015JB011979

Gutenberg, B., & Richter, C. F. (1944). Frequency of earthquakes in California. *Bulletin of the Seismological Society of America*, *34*(4), 185–188. https://doi.org/10.1785/bssa0340040185

Hainzl, S., Christophersen, A., Rhoades, D., & Harte, D. (2016). Statistical estimation of the duration of aftershock sequences. *Geophysical Journal International*, *205*(2), 1180–1189. https://doi.org/10.1093/gji/ggw075

Hatzigeorgiou, G. D., & Beskos, D. E. (2009). Inelastic displacement ratios for SDOF structures subjected to repeated earthquakes. *Engineering Structures*, *31*(11), 2744–2755. https://doi.org/10.1016/j.engstruct.2009.07.002

Huang, C., & Galasso, C. (2019). Ground-motion intensity measure correlations observed in Italian strong-motion records. *Earthquake Engineering & Structural Dynamics*, *48*(15), 1634–1660. https://doi.org/10.1002/eqe.3216

Iacoletti, S., Cremen, G., & Galasso, C. (2021). Advancements in multi-rupture time-dependent seismic hazard modeling, including fault interaction. *Earth-Science Reviews*, *220*, 103650. https://doi.org/10.1016/j.earscirev.2021.103650

Iacoletti, S., Cremen, G., & Galasso, C. (2022). Validation of the epidemic-type Aftershock sequence (ETAS) models for simulation-based seismic hazard assessments. *Seismological Research Letters*, *93*(3), 1601–1618. https://doi.org/10.1785/0220210134

Iacoletti, S., Cremen, G., Tomassetti, U., & Galasso, C. (2022b). Unsegmented long-term time-dependent modeling of the Nankai subduction zone (Japan). In *Proceedings of the 12th eleventh U.S. National conference on earthquake engineering* (Vol. (in print), p. 5). Earthquake Engineering Research Institute.

Iervolino, I., Giorgio, M., & Polidoro, B. (2014). Sequence-based probabilistic seismic hazard analysis. *Bulletin of the Seismological Society of America*, *104*(2), 1006–1012. https://doi.org/10.1785/0120130207

Kam, W. Y., Pampanin, S., & Elwood, K. (2011). Seismic performance of reinforced concrete buildings in the 22 February Christchurch (Lyttelton) earthquake. *Bulletin of the New Zealand Society for Earthquake Engineering*, *44*(4), 239–278. https://doi.org/10.5459/bnzsee.44.4.239-278

King, G. C. P., Stein, R. S., & Lin, J. (1994). Static stress changes and the triggering of earthquakes. *Bulletin of the Seismological Society of America*, *84*(3), 935.

Lanzano, G., Luzi, L., D'Amico, V., Pacor, F., Meletti, C., Marzocchi, W., et al. (2020). Ground motion models for the new seismic hazard model of Italy (MPS19): Selection for active shallow crustal regions and subduction zones. *Bulletin of Earthquake Engineering*, *18*(8), 3487–3516. https://doi.org/10.1007/s10518-020-00850-y

Leonard, M. (2010). Earthquake fault scaling: Self-consistent relating of rupture length, width, average displacement, and moment release. *Bulletin of the Seismological Society of America*, *100*(5A), 1971–1988. https://doi.org/10.1785/0120090189

Lolli, B., Randazzo, D., Vannucci, G., & Gasperini, P. (2020a). The homogenized instrumental seismic catalog (HORUS) of Italy from 1960 to present. *Seismological Research Letters*, *91*(6), 3208–3222. https://doi.org/10.1785/0220200148

Lolli, B., Randazzo, D., Vannucci, G., & Gasperini, P. (2020b). The homogenized instrumental seismic catalog (HORUS) of Italy from 1960 to present [Dataset]. Istituto Nazionale di Geofisica e Vulcanologia (INGV). https://doi.org/10.13127/HORUS .

Mai, P. M., & Thingbaijam, K. K. S. (2014). SRCMOD: An online database of finite-fault rupture models. *Seismological Research Letters*, *85*(6), 1348–1357. https://doi.org/10.1785/0220140077

Markhvida, M., Ceferino, L., & Baker, J. W. (2018). Modeling spatially correlated spectral accelerations at multiple periods using principal component analysis and geostatistics. *Earthquake Engineering & Structural Dynamics*, *47*(5), 1107–1123. https://doi.org/10.1002/eqe.3007

Marzocchi, W., & Taroni, M. (2014). Some thoughts on declustering in probabilistic seismic-hazard analysis. *Bulletin of the Seismological Society of America*, *104*(4), 1838–1845. https://doi.org/10.1785/0120130300

Matthews, M. V., Ellsworth, W. L., & Reasenberg, P. A. (2002). A Brownian model for recurrent earthquakes. *Bulletin of the Seismological Society of America*, *92*(6), 2233–2250. https://doi.org/10.1785/0120010267

McGuire, R. K. (2004). *Seismic hazard and risk analysis*. Earthquake Engineering Research Institute.

Meletti, C., Marzocchi, W., D'Amico, V., Lanzano, G., Luzi, L., Martinelli, F., et al. (2021). The new Italian seismic hazard model (MPS19). *Annals of Geophysics*, *64*(1), SE112. https://doi.org/10.4401/ag-8579

Mignan, A., Danciu, L., & Giardini, D. (2016). Considering large earthquake clustering in seismic risk analysis. *Natural Hazards*. https://doi.org/10.1007/s11069-016-2549-9

Mitchell-Wallace, K. (Ed.) (2017). *Natural catastrophe risk management and modelling: A practitioner's guide*. John Wiley and Sons, Inc.

Mori, F., Mendicelli, A., Moscatelli, M., Romagnoli, G., Peronace, E., & Naso, G. (2020). A new Vs30 map for Italy based on the seismic microzonation dataset. *Engineering Geology*, *275*, 105745. https://doi.org/10.1016/j.enggeo.2020.105745

Murru, M., Akinci, A., Falcone, G., Pucci, S., Console, R., & Parsons, T. (2016). M ≥ 7 earthquake rupture forecast and time-dependent probability for the sea of Marmara region, Turkey: Occurrence probability in Marmara Sea. *Journal of Geophysical Research: Solid Earth*, *121*(4), 2679–2707. https://doi.org/10.1002/2015JB012595

Ogata, Y. (1998). Space-time point-process models for earthquake occurrences. *Annals of the Institute of Statistical Mathematics*, *50*(2), 379–402. https://doi.org/10.1023/A:1003403601725

Ogata, Y., & Zhuang, J. (2006). Space–time ETAS models and an improved extension. *Tectonophysics*, *413*(1–2), 13–23. https://doi.org/10.1016/j.tecto.2005.10.016

Pace, B., Visini, F., & Peruzza, L. (2016). FiSH: MATLAB tools to turn *fault d*ata into seismic-hazard models. *Seismological Research Letters*, *87*(2A), 374–386. https://doi.org/10.1785/0220150189

Pagani, M., Monelli, D., Weatherill, G. A., & Garcia, J. (2014). The OpenQuake-engine book: Hazard (Technical Report no. 2014-08). *Global Earthquake Model (GEM)*.

Pantosti, D., D'Addezio, G., & Cinti, F. R. (1996). Paleoseismicity of the Ovindoli-Pezza fault, central Apennines, Italy: A history including a large, previously unrecorded earthquake in the middle ages (860–1300 A.D.). *Journal of Geophysical Research: Solid Earth*, *101*(B3), 5937–5959. https://doi.org/10.1029/95JB03213

Papadopoulos, A. N., Bazzurro, P., & Marzocchi, W. (2020). Exploring probabilistic seismic risk assessment accounting for seismicity clustering and damage accumulation: Part I. Hazard analysis. *Earthquake Spectra*, *37*(2), 803–826. https://doi.org/10.1177/8755293020957338

Porter, K., Field, E., & Milner, K. (2017). Trimming a hazard logic tree with a new model-order-reduction technique. *Earthquake Spectra*, *33*(3), 857–874. https://doi.org/10.1193/092616eqs158m

Potter, S., Becker, J., Johnston, D., & Rossiter, K. (2015). An overview of the impacts of the 2010–2011 Canterbury earthquakes. *International Journal of Disaster Risk Reduction*, *14*, 6–14. https://doi.org/10.1016/j.ijdrr.2015.01.014

Powers, P. M., & Field, E. H. (2013). Appendix O—gridded seismicity sources (Technical Report Nos. U.S. Geological Survey Open-File report 2013-1165-S, and California geological Survey special report 228-S).

Rovida, A., Locati, M., Camassi, R., Lolli, B., & Gasperini, P. (2020a). The Italian earthquake catalogue CPTI15 [Dataset]. Istituto Nazionale di Geofisica e Vulcanologia (INGV). https://doi.org/10.13127/DBMI/DBMI15.4

Rovida, A., Locati, M., Camassi, R., Lolli, B., & Gasperini, P. (2020b). The Italian earthquake catalogue CPTI15. *Bulletin of Earthquake Engineering*, *18*(7), 2953–2984. https://doi.org/10.1007/s10518-020-00818-y

Saltelli, A., Annoni, P., Azzini, I., Campolongo, F., Ratto, M., & Tarantola, S. (2010). Variance based sensitivity analysis of model output. Design and estimator for the total sensitivity index. *Computer Physics Communications*, *181*(2), 259–270. https://doi.org/10.1016/j.cpc.2009.09.018

Salvi, S., Cinti, F. R., Colini, L., D'Addezio, G., Doumaz, F., & Pettinelli, E. (2003). Investigation of the active Celano–L'Aquila fault system, Abruzzi (central Apennines, Italy) with combined ground-penetrating radar and palaeoseismic trenching. *Geophysical Journal International*, *155*(3), 805–818. https://doi.org/10.1111/j.1365-246X.2003.02078.x

Schwartz, D. P., & Coppersmith, K. J. (1984). Fault behavior and characteristic earthquakes: Examples from the Wasatch and San Andreas Fault zones. *Journal of Geophysical Research: Solid Earth*, *89*(B7), 5681–5698. https://doi.org/10.1029/JB089iB07p05681

Scotti, O., Visini, F., Faure Walker, J., Peruzza, L., Pace, B., Benedetti, L., et al. (2021). Which fault threatens me most? Bridging the gap between geologic data-providers and seismic risk practitioners. *Frontiers of Earth Science*, *8*, 750. https://doi.org/10.3389/feart.2020.626401

Šipčić, N., Kohrangi, M., Papadopoulos, A. N., Marzocchi, W., & Bazzurro, P. (2022). The effect of seismic sequences in probabilistic seismic hazard analysis. *Bulletin of the Seismological Society of America*, *112*(3), 1694–1709. https://doi.org/10.1785/0120210208

SSHAC. (1997). Recommendations for probabilistic seismic hazard analysis: Guidance on uncertainty and use of experts (Technical Report Nos. NUREG/CR–6372-Vol.1, UCRL-ID–122160, 479072). https://doi.org/10.2172/479072

Stepp, J. C. (1972). Analysis of completeness of the earthquake sample in the Puget Sound area and its effect on statistical estimates of earthquake hazard. In *Proceedings of 1st International Conference Microzonazion* (Vol. 2, pp. 897–910).

Stirling, M., McVerry, G., Gerstenberger, M., Litchfield, N., Van Dissen, R., Berryman, K., et al. (2012). National seismic hazard model for New Zealand: 2010 update. *Bulletin of the Seismological Society of America*, *102*(4), 1514–1542. https://doi.org/10.1785/0120110170

Toda, S., Stein, R. S., Reasenberg, P. A., Dieterich, J. H., & Yoshida, A. (1998). Stress transferred by the 1995 Mw = 6.9 Kobe, Japan, shock: Effect on aftershocks and future earthquake probabilities. *Journal of Geophysical Research: Solid Earth*, *103*(B10), 24543–24565. https://doi.org/10.1029/98JB00765

Utsu, T., Ogata, Y., S, R., & Matsu'ura (1995). The centenary of the Omori formula for a decay law of aftershock activity. *Journal of Physics of the Earth*, *43*(1), 1–33. https://doi.org/10.4294/jpe1952.43.1

Valentini, A., Pace, B., Boncio, P., Visini, F., Pagliaroli, A., & Pergalani, F. (2019). Definition of seismic input from fault-based PSHA: Remarks after the 2016 central Italy earthquake sequence. *Tectonics*, *38*(2), 595–620. https://doi.org/10.1029/2018TC005086

Visini, F., Meletti, C., Rovida, A., D'Amico, V., Pace, B., & Pondrelli, S. (2022). Updated area-source seismogenic model for seismic hazard of Italy. *Natural Hazards and Earth System Sciences Discussions*, 1–31. https://doi.org/10.5194/nhess-2022-60

Weatherill, G. A., Silva, V., Crowley, H., & Bazzurro, P. (2015). Exploring the impact of spatial correlations and uncertainties for portfolio analysis in probabilistic seismic loss estimation. *Bulletin of Earthquake Engineering*, *13*(4), 957–981. https://doi.org/10.1007/s10518-015-9730-5

Woessner, J., Laurentiu, D., Giardini, D., Crowley, H., Cotton, F., Grünthal, G., et al. (2015). The 2013 European seismic hazard model: Key components and results. *Bulletin of Earthquake Engineering*, *13*(12), 3553–3596. https://doi.org/10.1007/s10518-015-9795-1

Yaghmaei-Sabegh, S., Shoaeifar, P., & Shoaeifar, N. (2017). Probabilistic seismic-hazard analysis including earthquake clusters. *Bulletin of the Seismological Society of America*, *107*(5), 2367–2379. https://doi.org/10.1785/0120170031

Yeo, G. L., & Cornell, C. A. (2009). A probabilistic framework for quantification of aftershock ground-motion hazard in California: Methodology and parametric study. *Earthquake Engineering & Structural Dynamics*, *38*(1), 45–60. https://doi.org/10.1002/eqe.840

You, T., Wang, W., & Chen, Y. (2021). A framework to link community long-term resilience goals to seismic performance of individual buildings using network-based recovery modeling method. *Soil Dynamics and Earthquake Engineering*, *147*, 106788. https://doi.org/10.1016/j.soildyn.2021.106788

Yun, W., Lu, Z., Zhang, K., & Jiang, X. (2017). An efficient sampling method for variance-based sensitivity analysis. *Structural Safety*, *65*, 74–83. https://doi.org/10.1016/j.strusafe.2016.12.007

Zhuang, J., Werner, M. J., Zhou, S., Harte, D., & Hainzl, S. (2011). Basic models of seismicity: Spatiotemporal models. *Community Online Resource for Statistical Seismicity Analysis*. https://doi.org/10.5078/CORSSA-07487583